1

Computer-Aided Diagnosis for Acute Stroke in CT Images

Yongbum Lee, Noriyuki Takahashi and Du-Yih Tsai
Niigata University
Japan

1. Introduction

The mortality rate for cerebrovascular disease is approximately ten percents in all deaths in the world (World Health Organization [WHO], 2002). The cerebrovascular disease is a major cause of disability and is one of the three leading causes of death with heart disease and malignant neoplasm in several countries, e.g. Japan (Health and Welfare Statistics Association, 2004). Acute cerebral infarction is one of the major cerebrovascular diseases, and detection of its early signs is very important for survival and convalescence. Currently, computed tomography (CT) is still the most commonly used imaging modality in the diagnosis of acute cerebral infarction because of its wide availability and examination speed, though the advanced magnetic resonance (MR) imaging is superior to the non-enhanced CT in respect of sensitivity in the detection of cerebral ischemia within the first few hours after symptom onset (Adams et al., 2003, 2005). With the introduction of thrombolysis, much attention has been directed to identify early CT signs, which are subtle early signs of ischemic changes on CT images, over the last decade (Kummer et al., 1997; Wardlaw et al., 1999; Barber et al., 2000). Detection of early CT signs is of importance in middle cerebral artery (MCA) strokes within the first few hours of the onset of symptoms.
Computer-aided diagnosis (CAD) for detection of early CT signs must contribute to the improvement of diagnostic accuracy for acute stroke. Therefore, we developed some fundamental techniques to enhance/detect early CT signs. In this chapter, we describe two techniques to be used in CAD for acute stroke. By each technique, early CT signs are enhanced, visualized, detected and classified, respectively.

2. Enhancement of early CT signs

One of the notable early CT signs is the loss of gray-white matter interface, e.g. lenticular nuclei, due to the hypoattenuating appearance of gray matter structures (Tomura et al., 1988; Truwit et al., 1990). However, because of the subtle appearance of the loss of gray-white matter interface resulting from image noise, the radiologists may not be able to visually identify it (Schriger et al., 1998; Wardlaw & Mielke, 2005).
Recently technological innovation of CT units has dramatically advanced, so that image noise originated by the CT unit itself can be negligible. However, quantum noise due to X-ray quanta registered by the image detector cannot be prevented, even though using an ideal CT unit (Kaleder, 2000). The quantum noise degrades the visibility of low-contrast

structures such as normal gray-white matter interface on CT images. Under this condition, one can hardly recognize the normal gray-white matter interface on CT images, much less the loss of the gray-white matter interface due to cerebral ischemia. To solve this problem, it is necessary to improve the visibility of normal gray-white matter interface by removing or reducing the quantum noise with any ways. High-dose CT, for example, can reduce the quantum noise. However, this results in increasing patient radiation exposure. Hence, image processing techniques may become appropriate ways to reduce the quantum noise and consequently to improve the visibility of normal gray-white matter interface on CT images. Although various advanced digital filters for reducing image noise on CT images have been reported. However, these filters were mainly designed to deal with the reduction of radiation dose (Kalra et al., 2003; Kachelriess et al., 2001). In the present study, we focused on directly improving the visibility of normal gray-white matter interface on non-enhanced CT images by using a noise reduction filter. We believe that if noise is reduced, then the normal gray-white matter interface can be relatively enhanced. As a result, the loss of gray-white matter interface due to stroke could be more detectable. An exclusive smoothing filter is desirable to eliminate the quantum noise with almost no blurring of the edge of gray-white matter interface. To overcome this issue, an adaptive partial median filter (APMF) was proposed (Lee et al., 2007). The algorithm of APMF refers to Guis's contrast enhancement method (Guis et al., 2003) and is based on adaptive partial averaging filter (APAF) previously reported (Tsai et al., 2005; Lee et al., 2006; Takahashi et al., 2007). The distinction between APAF and APMF is simply the difference between "averaging" and "median" in a step of procedure. The APMF has a characteristic: noise can be reduced without degrading signal, i.e., edge. In the field of image processing, various image filtering techniques for noise reduction have been reported (Russ, 1995; Tukey, 1971; Davis & Rosenfeld, 1978; Wu et al., 1992; Ehrich, 1978; Lev et al., 1977; Wang et al., 1981; Nagao & Matuyama, 1978; Zamperoni, 1990; Xu et al., 2004; Kuan et al. 1985; Centeno & Haertel, 1997; Fischl & Shwarts, 1999; Westin et al., 2000; Schilham et al., 2006; Gijbels et al., 2006), and almost of them were edge-preserving smoothing techniques. The novel denoising technique, namely APMF, was compared to 14 conventional smoothing techniques by criterion-referenced performance study. Simulated CT images with gray-white matter interfaces were used for the study. Next, APMF was applied to a clinical database for application to actual clinical cases for preliminary observer performance study. Its usefulness was evaluated by receiver operator characteristic (ROC) analysis.

2.1 Adaptive partial median filter

The APMF is a specially designed filter with local median processing using a variable filter size and shape. The APMF's main steps are as follows, and illustrations corresponding to each step of APMF procedure are shown in Fig. 1.

Step 1. An averaging filter with $M \times M$ mask size is applied to the original image.

Step 2. A window image whose initial size is $W_{max} \times W_{max}$ is assigned from the original image after the averaging filter. W_{max} is a positive odd number from 3.

Step 3. A mask image is generated by assigning a binary mask value 0 if $|I(i, j)-I(i_c, j_c)|>T$, and by assigning a binary mask value 1 if $|I(i, j)-I(i_c, j_c)| \leq T$. $I(i_c, j_c)$ and $I(i, j)$ are defined as the pixel value of the center pixel and the pixel value of an arbitrary pixel in the window image, respectively.

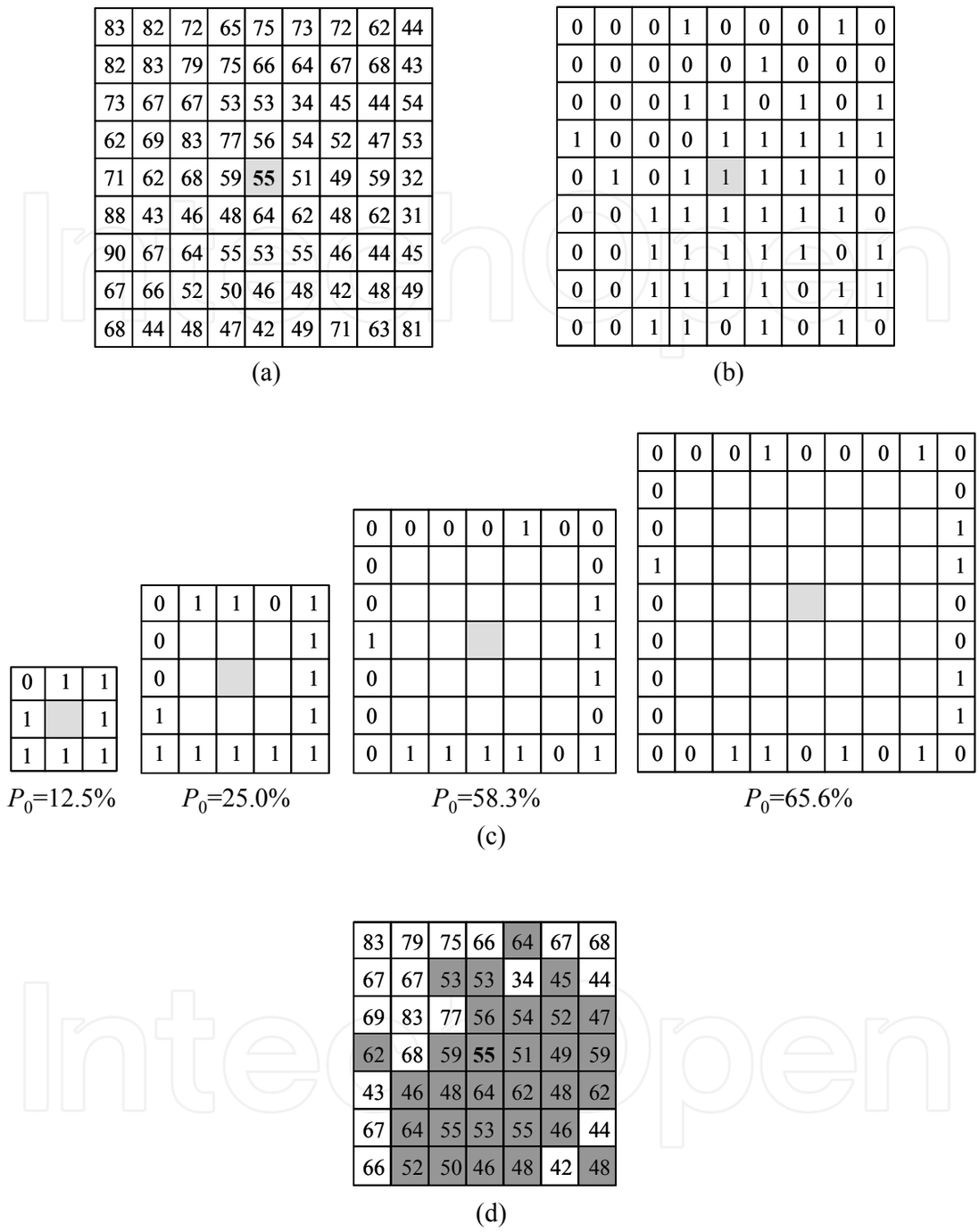

Fig. 1. An example corresponding to each step of APMF procedure. (a) A window image (W_{max}=9) in Step 2. (b) Assigned mask image from (a) in case of T=10 in Step 3. (c) Calculation of the percentage of P_0 of external area at W=[3, 5, 7, 9] in Step 4. When P=60%, W=7 are determined as actual window size. (d) Median value obtained from pixel values (in dark gray pixels) corresponding with mask value 1 in the mask image (W=7) replaces the center pixel value [$I(i_c, j_c)$=55 changes to $I(i_c, j_c)$=53].

Step 4. For each window size $W \times W$ [W = 3, 5, ...,W_{max}], the percentage P_0 of 0 in the mask image is computed over the region of external area of each window image. Actual window size is determined when the percentage P_0 is not greater than P%, and is closest to P%.

Step 5. Finally, a median value is obtained from the pixel values $I(i, j)$ corresponding with mask value 1 in mask image, and the median value is used as output value at the center pixel value $I(i_c, j_c)$.

Step 6. Steps 2–5 are performed at each pixel.

Step 1 is related to differentiating between the object pixel value $I(i_c, j_c)$ and the surrounding pixel value $I(i, j)$ described in Step 3. As noise superimposed on the object pixel has to be initially reduced, otherwise the APMF will not perform well. Step 3 is based on an assumption that variation of pixel values due to noise is smaller than the difference of pixel values due to signal, and is an important process to distinguish between noise and signal components. In Step 4, actual window size will be small to enhance the quality of edge preserving if there are many pixels with pixel values larger than T in window image. In contrast, the actual window size will be large to enhance the noise reduction rate if pixel values in window image are almost uniform. As for APAF, "median" is just replaced to "averaging" in Step 5.

The performance of the APMF depends on parameters M, W_{max}, T and P. In particular, T is very important parameter because it determines rough boundary of object, e.g. lenticular nuclei on a CT image. T distinguishes object region (mask value 1) and background region (mask value 0). Then only pixel values in object region are used for computation. It means that the APMF is able to reduce local noise while preserving edge components between object and background regions. Therefore, T for application to clinical images was obtained by a simulation study described in the next section. The other parameters of M=5, W_{max}=13, and P=60 were determined using the rule of trial and error on simulated images to be described in the next section.

2.2 Objective performance test

The simulation study has two purposes. One is to determine an adequate parameter of T for application to clinical CT images. The other one is to validate the superiority of the APMF by comparing with conventional smoothing techniques. Composite images with simulated white matter (SWM) and simulated gray matter (SGM) were used for this simulation. First, in order to obtain the simulated SWM, cylindrical phantom which was Catphan CT phantom CTP486 made by The Phantom Laboratories, Inc. was scanned by CT device which was Somatom Volume Zoom made by Siemens-Asahi Medical Technologies Ltd.. Then, the SGM was put on the CT image. Concretely, 3~6HU (Hounsfield Unit) was added to the SWM by computation because the contrast of normal gray-white matter interface was approximately 6HU, and the contrast of ischemic gray-white matter interface deteriorated to approximately 3HU. Fig.2 shows a simulation image and its sketch.

The size of simulation image shown in Fig.2 is 300×300 pixels. This is a part of original image whose size is 512×512 pixels. Edge slope between SWM and SGM on the dotted line in sketch of Fig.2 has been generated as shown in Fig.3. C_x in Fig.3 corresponds to the abscissa of the dotted line in sketch of Fig.2. The *cnt* in Fig.3 corresponds to the contrast between SWM and SWM, which is 3~6HU. The CT scan specifications were Tube Voltage 120kV, Tube Current 200~400mAs, Slice Thickness 10mm, FOV (field of view) 250mm, and matrix size 512×512. The phantom was scanned ten times under the same condition, and

then ten composite images were generated under the same condition to restrain variation of evaluation values that will be described in the next paragraph. The total number of simulation images was 120 which was obtained by 4 contrast levels (3~6HU, interval of 1 HU) × 3 noise levels (200~400mAs, interval of 100mAs) × 10 scans.

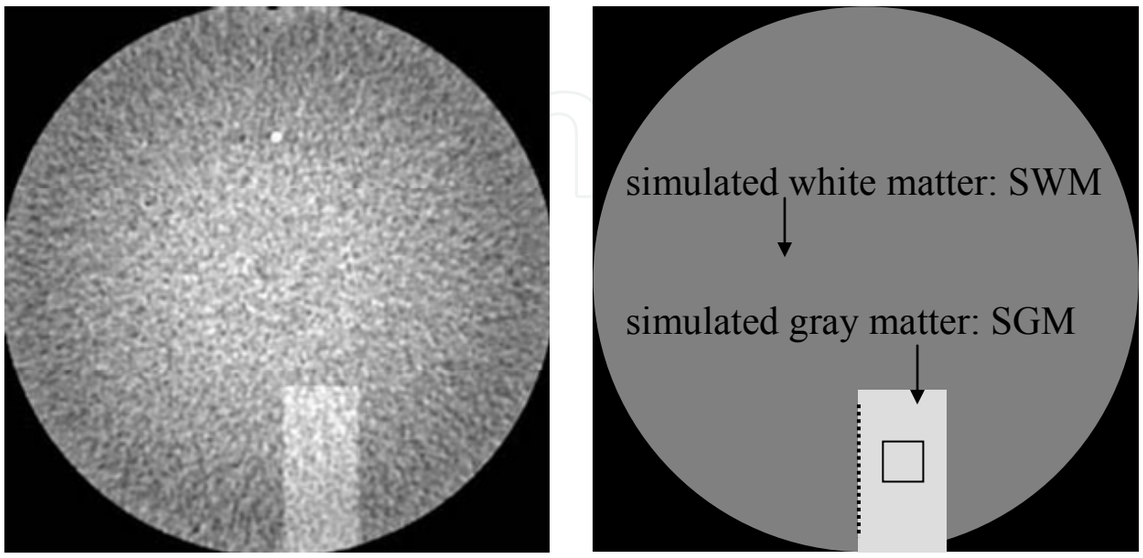

Fig. 2. A simulation image (left: 400mAs, 6HU) and its sketch (right). Dotted line in the sketch suggests a vertical edge line of 80 pixels length for ESR calculation. Its horizontal coordinate value is C_x. Square in the sketch suggests a region for SDR calculation. Its size is 20×20 pixels.

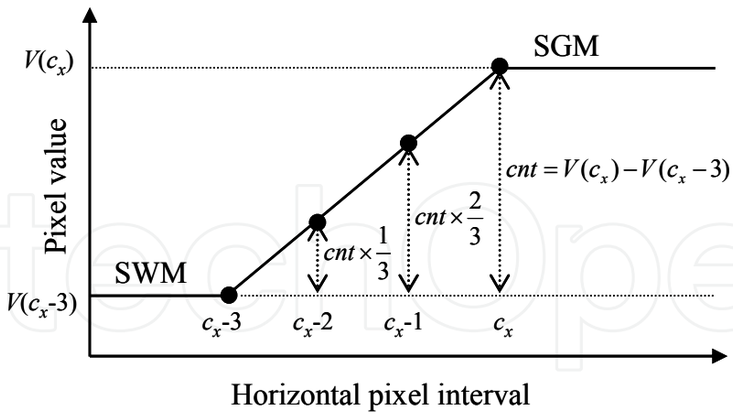

Fig. 3. Explanatory diagram with regard to edge slope of SGM-SWM interface.

The standard deviation rate (SDR) and edge slope rate (ESR) were used as two criteria for measuring the performance of the APMF and the conventional smoothing techniques. The standard deviation of the pixel values in a specified area, which was used to quantify the degree of noise reduction, was obtained from a region of 20×20 pixels on the SGM, as shown in Fig.2. To investigate the extent of edge preserving, edge slope rate was calculated from an average profile of pixel values, which was measured at the horizontal direction with respect

to the edge on the dotted line shown in Fig.2. The standard deviation rate was computed by Equation (1).

$$SDR(\%) = \left(SD_{org} - SD_{prc}\right) \Big/ SD_{org} \times 100 \tag{1}$$

SD_{org} is an average standard deviation calculated from ten original composite images, and SD_{prc} is an average standard deviation calculated from ten processed images. The edge slope rate was computed by Equation (2).

$$ESR(\%) = ES_{prc} \Big/ ES_{org} \times 100 \tag{2}$$

ES_{org} is an average edge slope value calculated from ten original composite images, and ES_{prc} is an average edge slope value calculated from ten processed images. Those are defined as Equation (3) and as shown in Fig.3. High SDR means that the noise is decreased well. High ESR means that the edge is highly preserved.

$$ES = \left\{V\left(C_x\right) - V\left(C_x - 3\right)\right\} \Big/ 3 \tag{3}$$

The APMF was compared to 14 conventional smoothing filters, namely, averaging filter (AF) (Russ, 1995), median filter (MF) (Tukey, 1971), gaussian filter (GF) (Russ, 1995), k-nearest neighbor averaging (KNNA) (Davis & Rosenfeld, 1978), k-nearest neighbor median (KNNM) (Wu et al. 1992), hysteresis smoothing (HS) (Ehrich, 1978), edge and line weights smoothing (ELWS) (Lev et al., 1977), contrast sensitive weights smoothing (CSWS) (Lev et al., 1977), gradient inverse weighted smoothing (GIWS) (Wang et al., 1981), Nagao's edge preserving smoothing (EPS) (Nagao & Matuyama, 1978), adaptive rank order filter (AROF) (Zamperoni, 1990), adaptive two pass median filter (ATPMF) (Xu et al., 2004), adaptive noise smoothing filter (ANSF) (Kuan et al., 1985), and adaptive partial averaging filter (APAF) (Tsai et al., 2005, Lee et al., 2006, Takahashi et al., 2007) which was a basis of APMF. The SDR and ESR of each method were calculated from the processed composite images obtained by varying Tube Current (200, 300, 400mAs) and the contrast (3, 4, 5, 6HU) between SGM and SWM. As a sample of results, Fig.4 shows graphs of SDR and ESR in the case of 400mAs, 6HU. For those methods with variable filter size (FS), namely, AF, MF, GF, KNNA, KNNM, AROF, ATPMF and ANSF, the filter size was used as variable of the horizontal axis on the graphs. This means that SDR and ESR were calculated by varying filter size. For those methods with fixed filter size, namely, ELWS, CSWS, GIWS, and EPS, the number of iteration (NI) was used as variable of the horizontal axis on the graphs. This means that SDR and ESR were calculated by varying the number of iteration. HS has an only parameter of *Width* which is an established hysteresis cursor size, and is at least equal to the size of the largest waveform peak or valley to be removed (Ehrich, 1978). Therefore, the Width was used as variable of the horizontal axis on the graph of HS. The parameters of APAF are the same with the parameters of APMF because the difference between APAF and APMF is only whether the output value at the center pixel value $I(i_c, j_c)$ in Step 5 is the averaging value or the median value. Therefore, the parameter T was used as variable of the horizontal axis on the graph of APAF, as that of APMF. Other parameters as shown in Table 1, which were σ of GF and CSWS, a and b of ATPMF, and k of KNNA and KNNM, were determined experimentally by referring to the respective literatures.

Method	Parameters	SDR(%)	ESR(%)
Adaptive partial median filter (APMF)	M=5, Wmax=13, P=60, T=3	76.0	71.7
Adaptive partial averaging filter (APAF) [16],[17]	M=5, Wmax=13, P=60, T=3	75.6	64.0
Averaging filter (AF) [18]	FS=13	76.4	23.6
Median filter (MF) [19]	FS=15	76.1	33.1
Gaussian filter (GF) [18]	FS=55, σ=(FS-1)/4	76.1	31.2
Adaptive two pass median filter (ATPMF) [27]	FS=13, a=1, b=1	75.4	49.9
Adaptive noise smoothing filter (ANSF) [28]	FS=15	76.0	30.6
Edge and line weights smoothing (ELWS) [23]	NI=93	76.0	51.4
Contrast sensitive weights smoothing (CSWS) [23]	NI=20, σ=50	76.0	31.3
Hysteresis smoothing (HS) [22]	Width=5	35.0	69.7
k-nearest neighbor averaging (KNNA) [20]	FS=37, k=FS×FS/2	40.7	72.0
k-nearest neighbor median (KNNM) [21]	FS=31, k=FS×FS/2	47.9	71.5
Adaptive rank order filter (AROF) [26]	FS=7, k=eq.(6) in [26]	54.0	68.7
Gradient inverse weighted smoothing (GIWS) [24]	NI=352	49.5	71.7
Edge preserving smoothing (EPS) [25]	NI=10	20.1	86.7

Table 1. List of compared methods and comparison results.

Table 1 shows specific values of SDR and ESR extracted from the graphs in Fig.4. The specific values were based on SDR and ESR of APMF at T=3. We supposed that T=3 was the best value of T because ESR at T=3 was highest, and SDR at T=3 was almost highest. The details of this topic will be described in the next paragraph. In regard to AF, MF, GF, ELWS, CSWS, ATPMF, ANSF and APAF, the values of ESR were selected out when the values of SDR became closest to the SDR (76.0%) of APMF. In regard to the others that were KNNA, KNNM, HS, AROF, GIWS and ESP, the values of SDR were selected out when the values of ESR became closest to the ESR (71.7%) of APMF because the values of SDR did not become close to the SDR of APMF. In Table 1, highest ESR was 71.7% of APMF at the almost same SDR, and then in order, it was 64.0% of APAF, 51.4% of ELWS, and 49.9% of ATPMF. The ESR of the others, which were AF, MF, GF and CSWS, were less than 34.0%. In comparison in a condition of almost same ESR, highest SDR was 76.0% of APMF, and then the SDR of the others, which were KNNA, KNNM, HS, AROF, GIWS and EPS, were less than 55.0%. The processed images by each method with parameters shown in Table 1 are shown in Fig.5. These are parts of processed images around SGM-SWM interface. The image qualities are well consistent with the criterion values shown in Table 1. These comparison results clearly indicated that the APMF had the highest performance among the compared methods. The all results in conditions by varying Tube Current (200, 300, 400mAs) and the contrast (3, 4, 5, 6HU) between SGM and SWM had the same tendencies (Fig.6).

Clinical brain CT images used in this study were scanned by the ProSeed Accell made by GE Yokogawa Medical System, whose specifications were Tube Voltage 120kV, Tube Current 400mAs, Slice Thickness 10mm, FOV 250mm, and matrix size 512×512. These specifications correspond to those for sample graph of APMF shown in Fig.4. Therefore, an adequate T could be determined by referring to the simulation result of APMF as shown in Fig.4. SDR almost stop increasing from T>3, and ESR began to decrease sharply from T>3 (the peak at T=3).

Fig.7 shows the processed images obtained by varying the threshold value T [0, 1, 2, 3, 4, 5, 6] of APMF. The APMF image at T=3 looks very well with regard to edge sharpness and noise reduction. The APMF images at T=0, 1, 2 are insufficient on the degree of noise reduction, and the APMF images at T=4, 5, 6 are too blurry. Considering these data, T=3

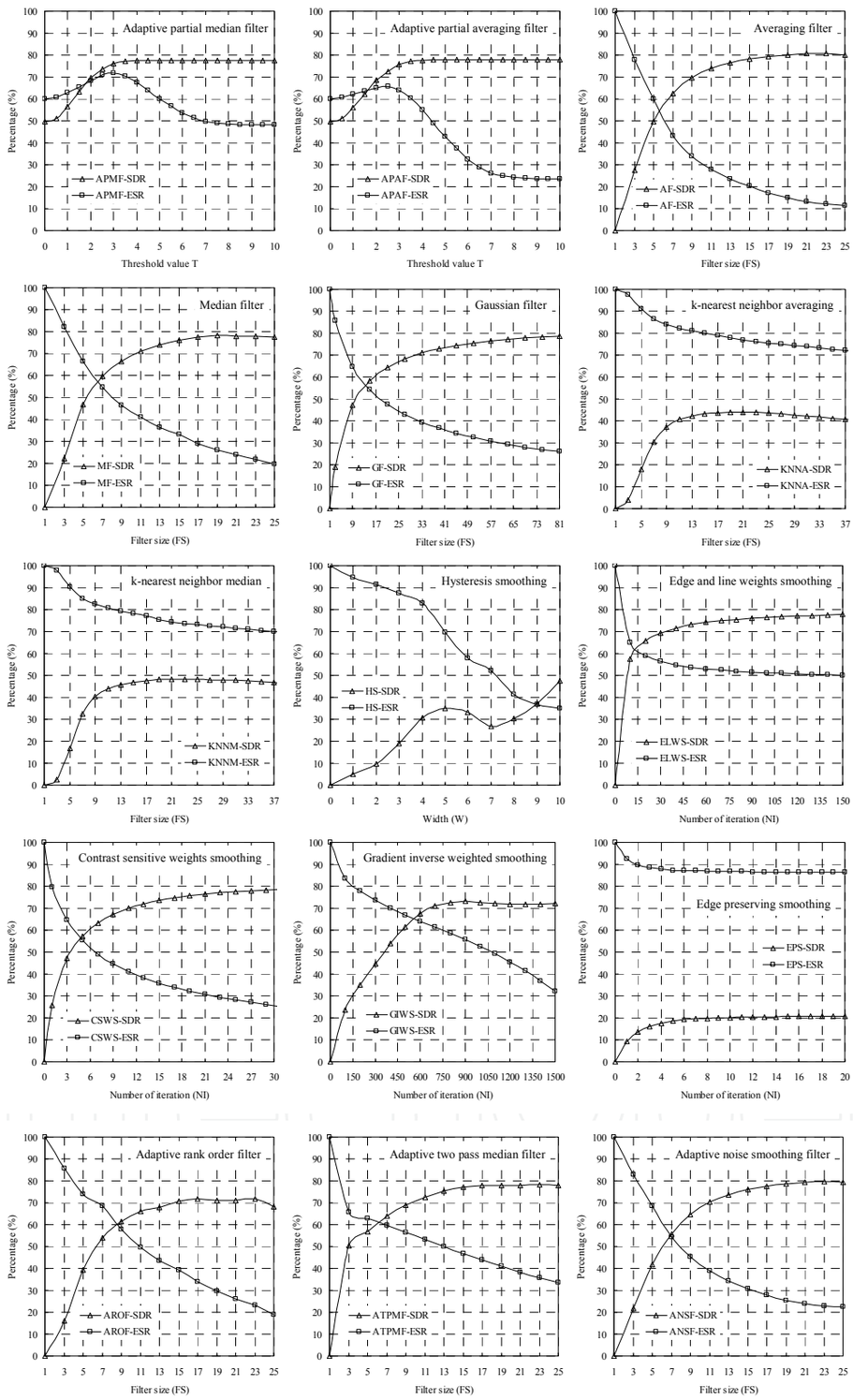

Fig. 4. Graphs of SDR and ESR obtained from simulation images in condition of 400mAs, 6HU.

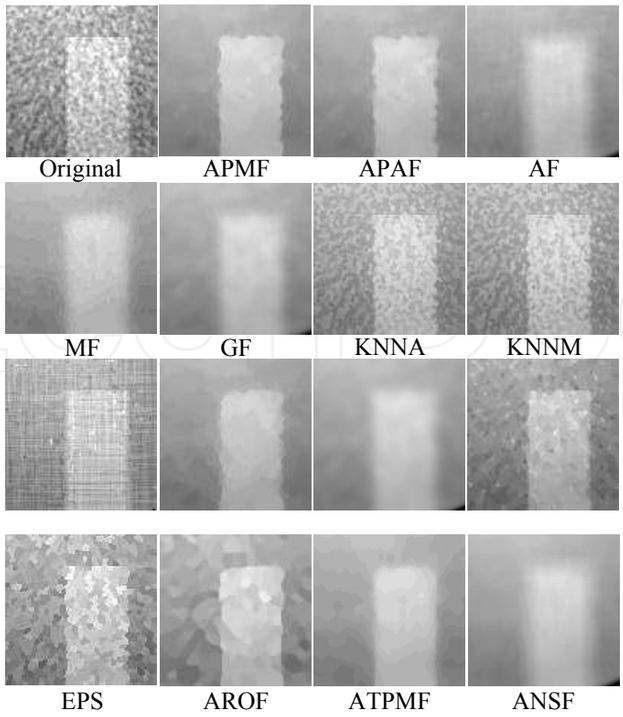

Fig. 5. Various processed images (400mAs, 6HU) with parameters in Table 1.

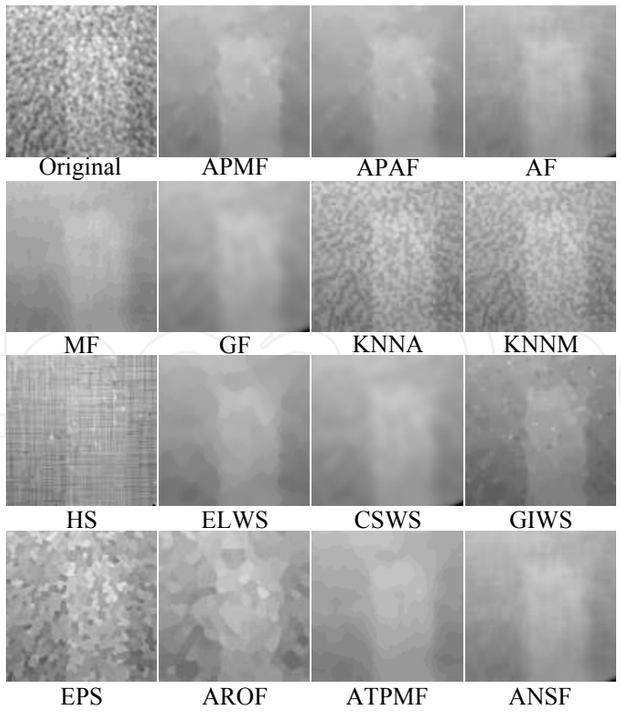

Fig. 6. Various processed images (400mAs, 3HU) corresponding to either SDR≈75% or ESR≈49%. These numerical values were obtained from APMF images.

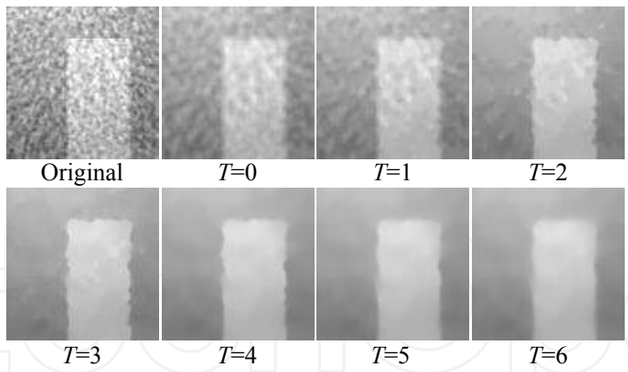

Fig. 7. APMF processed images (400mAs, 6HU) by varying T.

might be an adequate threshold value in the condition of 400mAs and on the assumption that the contrast of gray-white matter interface on clinical brain CT image was approximately 6HU. Therefore, *T*=3 was determined as an adequate parameter for applying to clinical CT images in this study.

2.3 Subjective performance test

The APMF at *T*=3 was applied to 51 non-enhanced brain CT images which consisted of 18 abnormal images and 33 normal images, and then observer study with ROC analysis was performed by 4 radiologists. The abnormal images were obtained from 18 patients (mean age, 74 years) with acute (within 5 hours) cerebral infarction, and all of them showed subtle loss of the gray-white matter interface in the cortical ribbon and/or in the lentiform nucleus. The normal images were obtained from 33 control patients (mean age, 68 years). Two samples of abnormal cases used in this study are shown in Fig.8. A sample supplies three CT images, which are original image, APMF image and follow-up image obtained several days after the onset of symptoms. The original image of case 1 illustrated on the upper left in Fig.8 was obtained in an 83-year-old-female with right hemiplegia at 2.4 hours after stroke onset. The APMF image shows that the loss of the gray-white matter interface at the left lentiform nucleus, the so-called obscured outline of the lentiform nucleus, is clearly detectable (arrows). The outline of the right normal lentiform nucleus is obviously visible compared to the corresponding contralateral one. The follow-up image demonstrates infarction in the left middle cerebral artery (MCA) and anterior cerebral artery (ACA) distributions. The original image of case 2 illustrated on the lower left in Fig.8 was obtained in an 83-year-old-male with right hemiplegia at 1.5 hours after stroke onset. The APMF image shows that the loss of the gray-white matter interface of posterior part of the left lentiform nucleus is clearly detectable. The follow-up image demonstrates infarction in the left middle cerebral artery (MCA) and posterior cerebral artery (PCA) distributions. Two samples vividly indicated that early CT signs of acute cerebral infarction were remarkably enhanced in the APMF images.

Four radiologists including two attending radiologists (years of experience, 14-18 years) and two radiology resident (years of experience, 1-3 years) independently interpreted the cases on the monitor for this observer study. First diagnostic decisions of them were determined by interpreting only original images. Window width (WW) and window level (WL) were free in their interpreting. Although there were some reports that diagnostic accuracy would be improved by using narrow WW in interpreting on the monitor (Lev et al., 1999), narrow

WW enhances not only edge such as gray-white matter interface but quantum noise in non-enhanced CT image. Therefore, default WW and WL for original images were 80 and 35HU, respectively, because it was the general condition for diagnosis in radiologist's daily work in Japan. After first interpreting, they could correct their decisions by reinterpreting both original and the APMF images. Default WW and WL for the APMF images were 20 and 35HU, respectively. Narrow WW was used for the APMF images as default condition because quantum noises were sufficiently decreased by APMF. Narrow WW after decreasing noises in the APMF images enhances only edges such as gray-white matter interface. The radiologists indicated their confidence rating regarding the presence or absence of early CT sign on each case. The scale of confidence rating ranged from 0 to 100. A computer program (LABMRMC; Charles E. Metz, University of Chicago) (Dolfman et al., 1992) was used for obtaining ROC curves and the statistical significance of the difference between the ROC curves by only original images and by original images with APMF images.

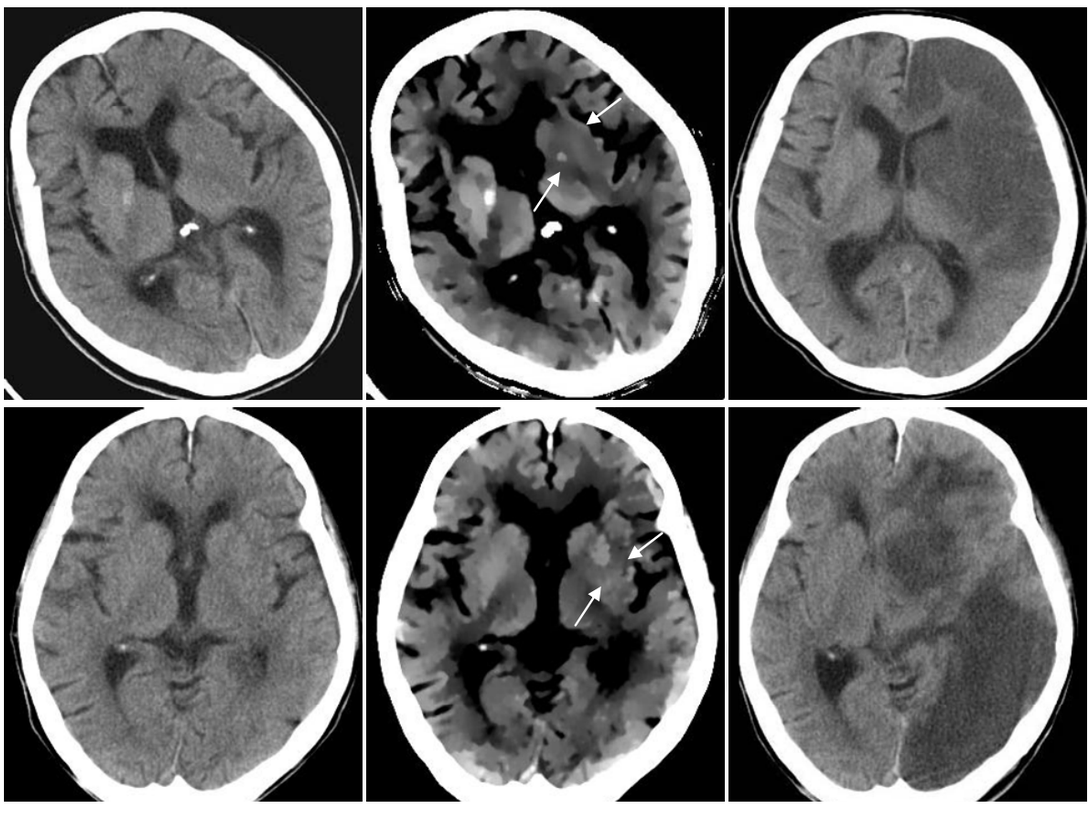

Fig. 8. Two examples of abnormal cases. Lefts are original images (WL=35, WW=80). Middles are APMF images (WL=35, WW=20). Rights are follow-up images obtained several days after the onset of symptoms (WL=35, WW=80). Arrows indicate obscuration of the lentiform nucleus.

The area under the ROC curves plotted in the unit square (A_z) was calculated for each fitted curve. The overall performance is illustrated in Table 2 and Fig.9. Table 2 shows the A_z values without the APMF images and with the APMF images for each radiologist. Figure 9 shows the average ROC curves of four radiologists without the APMF images

and with the APMF images. The performance of all observers was improved when the APMF image was used. The average A_z values for all radiologists increased from 0.876 without the APMF images to 0.926 with the APMF images, and this difference was statistically significant (P=0.04). This preliminary result of observer study is suggesting that the APMF can be an useful technique for diagnosis of acute cerebral infarction in non-enhanced CT images. The observer performance study using much more cases and by more observers would be required to more clearly prove the usefulness of APMF to clinical cases in the future work. We believe that the results from two performance studies demonstrate the usefulness of APMF.

	Az value	
Observer	Only original images	Original + APMF images
A	0.912	0.952
B	0.881	0.922
C (resident)	0.842	0.914
D (resident)	0.866	0.916
Mean	0.876	0.926

Note.-The difference was statistically significant with a *P* value of 0.04.

Table 2. A_z values for each observer.

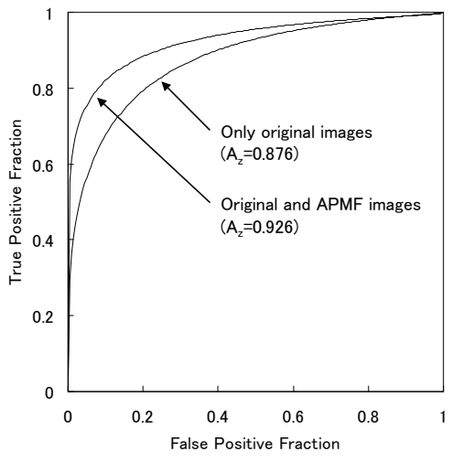

Fig. 9. Average ROC curves of four radiologists for diagnosis of acute stroke from brain CT images without the APMF images and with the APMF images.

3. Detection of hypoattenuation in CT images

Unenhanced computed tomographic (CT) imaging still plays an important role in the assessment of eligible patients for receiving thrombolytic therapy for hyperacute ischemic stroke, because of its wide accessibility and convenience, although diffusion-weighted MR imaging (DWI) in acute stroke has been supported (Adams et al., 2003, 2005). Patients showing large ischemic lesions (parenchymal hypoattenuation or brain swelling) on CT images have a high risk of fatal hemorrhagic complications after thrombolytic therapy (Kummer et al., 1997; Barber et al., 2000; Kalafut et al., 2000). Therefore, quantification of

the extent of areas of ischemic lesions appeared on CT images is mandatory to avoid the risk. However, because the detection of hypoattenuation (a subtle attenuation change of ischemic brain tissue) is difficult, inter-rater homogeneity is poor in the assessment of the extent of areas of ischemic lesions (Fiebach et al. 2002). Thus, the detectability of hypoattenuation largely depends on the skill and experiences of the interpreters (Schriger et al., 1998; Wardlaw et al., 2005). To cope with this issue, a quantitative CT scoring system, the Alberta Stroke Programme Early CT Score (ASPECTS) (Barber et al., 2000), has been proposed to help interpreters in quantifying the extent of ischemic lesions in the territory of the middle cerebral artery (MCA). However, the sensitivity for the detection of acute stroke was less than 50% on unenhanced CT images, even when the ASPECTS method was used (Camargo et al., 2007).

Recently, a *z*-score mapping method on the basis of a voxel-by-voxel analysis has been developed to assist interpreters in quantifying the extent of hypoattenuation regions of hyperacute ischemic stroke on unenhanced CT images (Takahashi et al., 2010a, 2010b). The method was applied to patients with the MCA territory infarction within 3 hours of symptom onset for its performance test. The result of the test has shown that the method is effective in the visualization of hypoattenuation areas. However, observer performance study on the quantification of the extent of hypoattenuation regions of hyperacue stroke by use of the method has not yet been made.

We evaluated the usefulness of the *z*-score mapping method on neuroradiologists' performance in the quantification of the extent of hypoattenuation regions of hyperacute stroke using the ASPECTS score system. Accuracies of the quantification without and with the *z*-score maps were calculated to evaluate observers' performance in the quantification of the extent of hypoattenuation regions. Moreover, receiver operating characteristic (ROC) analysis was used to evaluate observers' performance in the detection of focal hypoattenuation.

3.1 Z-score mapping method

Z-score mapping method (Takahashi et al., 2010a, 2010b) consisted of five main steps, i.e., anatomic standardization, the construction of a normal reference database, calculation of the *z*-score, the elimination of cerebrospinal fluid (CSF) areas, and display of *z*-score maps.

First, all data sets were transformed into a standard brain atlas using Statistical Parametric Mapping 2 (SPM2) software (The Welcome Department of Cognitive Neurology, London, United Kingdom) (Friston et al., 1995; Ashbumer & Friston, 1999). The matrix size used for normalization was 79×95×69 voxels (2-mm anisotropic voxel size). Processed data sets were then smoothed with a 4-mm full width at half maximum isotropic Gaussian kernel.

Second, two normal data sets for reference were constructed by computing the averages and standard deviations (SDs) of image voxel values from the normalized CT database. The CT database was comprised of 28 normal controls.

Third, the *z*-score was calculated on a voxel-by-voxel basis as shown in Fig.10 and was defined as Equation (4).

$$Z-score_{(x,y,z)} = \left(C_{mean(x,y,z)} - Input_{(x,y,z)}\right) \Big/ N_{SD(x,y,z)} \tag{4}$$

$C_{mean}(x, y, z)$ and $N_{SD}(x, y, z)$ represent the mean and standard deviation of the normal reference data at the coordinate of (x, y, z), respectively. $Input(x, y, z)$ is the value of spatially

normalized patient data set at the same coordinate system. Before the calculation of *z*-scores, an offset was used to remove variation among patients in attenuation coefficients of the normal brain parenchyma on unenhanced CT images.

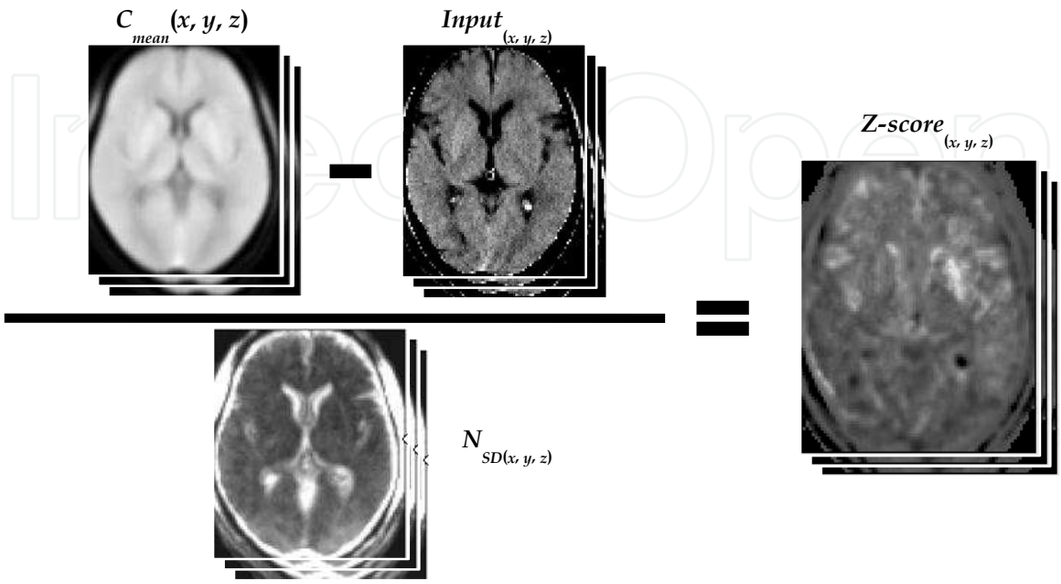

Fig. 10. Calculation of *z*-score for input CT scan

In the fourth step, CSF areas which may give rise to false-positive (FP) results, were eliminated from *z*-score data set by use of a gray-scale thresholding technique (Fig.11). Note that CT values of CSF areas may be lower than those of hypoattenuation areas. Therefore, after using adaptive thresholding, the CSF areas can be removed while maintaining hypoattenution areas. After the elimination of CSF areas, the area of the brain parenchyma except the MCA territory was also removed from the *z*-score data set.

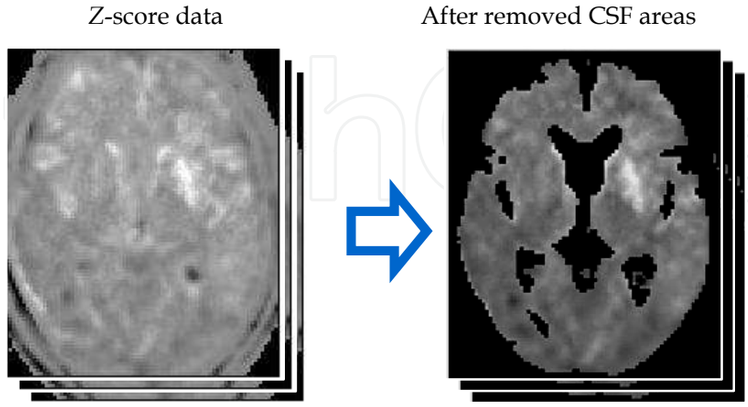

Fig. 11. Elimination of false positive areas.

Finally, the normalized input CT data set and the *z*-score map were reconstructed with a slice thickness of 4 mm. The *z*-score map was then superimposed on the normalized CT data set and was color-coded to reflect ranges of *z*-scores, as shown in Fig.12. Small

clusters having 50 voxels or less were removed from the *z*-score map before displaying the *z*-score map.

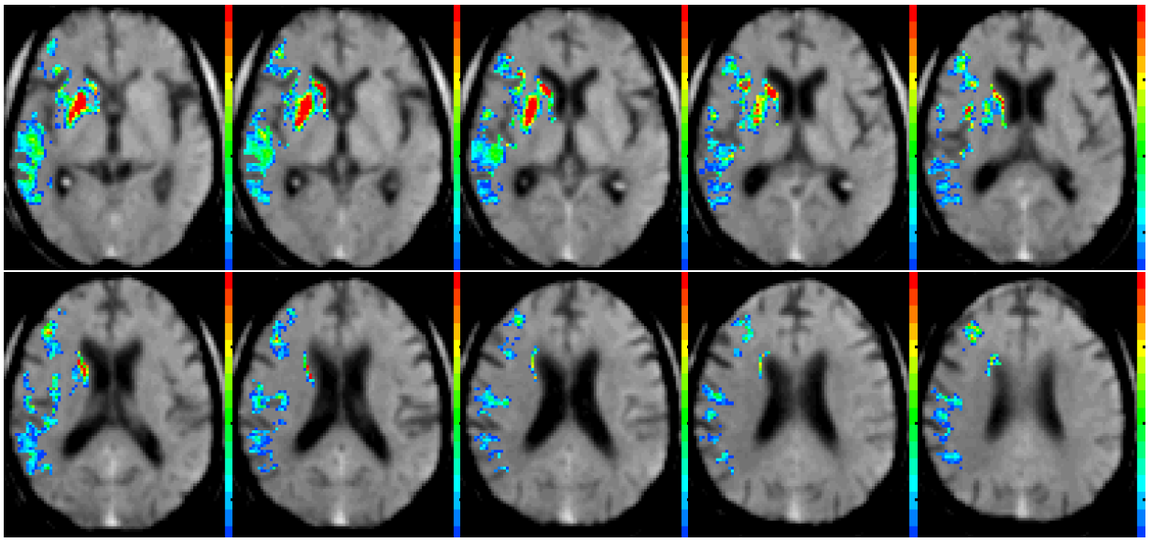

Fig. 12. Display of *z*-score maps.

3.2 Observer performance study

Data from 34 consecutive patients with embolic infarction in the MCA territory stroke who underwent unenhanced CT scan at Sendai City Hospital, Sendai, Japan, between April 2007 and December 2008 were collected for this study. From the 34 collected CT files, 21 patients were selected using the following inclusion criteria: (1) the first CT scan was performed within 3 hours after stroke onset, and (2) no patients had evidence of old infarctions. The 21 patients consisted of 14 men and 7 women (age range, 46-92 years; mean age, 66.5 years). The median National Institute of Health Stroke Scale score was 12 (range, 1-27) in the 21 patients. All patients underwent the first unenhanced CT scan within 3 hours (mean, 1.86 hours; range, 0.67-3 hours) after the onset of stroke ictus. All images were acquired using a 16-slice multidetector CT scanner (Emotion16; Siemens Medical Solutions, Forchheim, Germany). At our institution, CT scans are routinely obtained using a matrix size of 512×512 and a field of view of 230 mm, with 4.8-mm contiguous sections. Figure 13 shows 10 ASPECTS-defined regions in the MCA territory on 2 standardized axial section images. These regions included the lentiform nucleus (L), insula (I), caudate nucleus (C), internal capsule (IC), anterior inferior frontal lobe (M1), temporal lobe (M2), inferior parietal and posterior temporal lobe (M3), anterior superior frontal lobe (M4), precentral and superior frontal lobe (M5), and superior parietal lobe (M6). To constitute a criterion standard of hypoattenuation region on unenhanced CT images for the selected 21 patients, 2 neuroradiologists (31 and 19 years of neuroimaging review experience, respectively) determined criterion standard regions on unenhanced CT images in consensus. Hypoattenuation was defined as an area of abnormally low density of brain structures relative to attenuation of the contralateral hemisphere. The neuroradiologists identified the existence of hypoattenuation in each of the 10 regions of the MCA territory on the cerebral hemisphere suspected of hyperacute ischemic stroke in each patient by referring followup CT images. Diffusion-weighted MR images were used only for help in determining the

criterion standard if necessary. Three of the 21 patients presented no hypoattenuation regions on CT images but presented hyperintense lesions on diffusion-weighted MR images. The mean number of hypoattenuation regions per patient was 3.2 (range, 0**Y**9) in the 21 patients. Figure 14 shows the distribution of the number of hypoattenuation regions identified by the 2 neuroradiologists from the 21 patients.

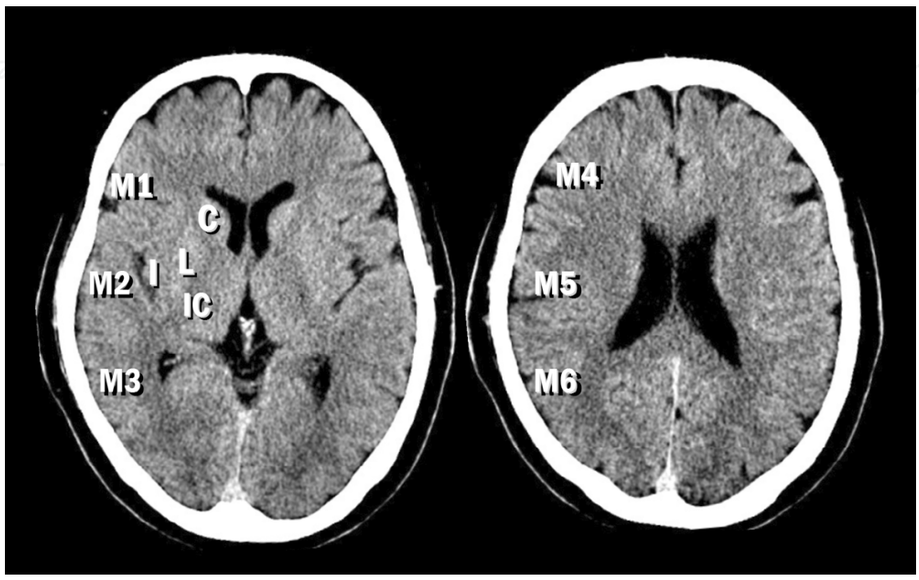

Fig. 13. Ten Alberta Stroke Programme Early CT Score (ASPECTS)-defined regions in the MCA territory for the performance evaluation on unenhanced CT images. These regions include lentiform nucleus (L), insula (I), caudate nucleus (C), internal capsule (IC), anterior inferior frontal lobe (M1), temporal lobe (M2), inferior parietal and posterior temporal lobe (M3), anterior superior frontal lobe (M4), precentral and superior frontal lobe (M5), and superior parietal lobe (M6).

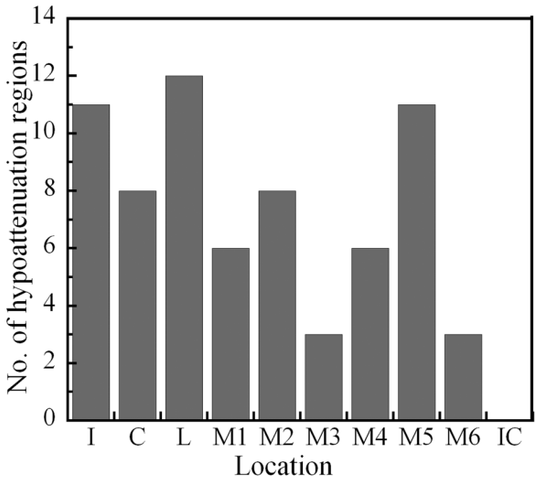

Fig. 14. Distribution of the number of hypoattenuation regions identified by two neuroradiologists from 21 patients.

Five neuroradiologists (years of experience 9-31 years) took part in the observer performance study. The two of them, who selected the patients, did not participate as an observer. All observers were blinded to all clinical and patient information, except that the information about the side of the hemisphere with stroke symptoms was provided. We used a sequential test method (Uozumi et al., 2001). Each observer first viewed CT images only for the initial rating, and then viewed both the original and the *z*-score maps for the second rating. During the rating process, the observers were asked to indicate their confidence level regarding the presence of parenchymal hypoattenuation at each of the 10 regions in the affected hemisphere of each patient by using a continuous rating scale (Metz et al., 1998). Each observer reviewed randomly the 21 patients, and rated his/her confidence level for the 210 regions of the 21 patients.

Before the observer test, each observer underwent a training session with four training cases to become familiar with the characteristics of *z*-score maps and the test procedure. The four training cases were not included in the observer performance study. The procedure that observers undertook is described as follows: (1) unenhanced CT images were displayed on a color monitor without *z*-score maps; (2) each observer rated the confidence level in the presence or absence of hypoattenuation in each of the 10 locations of every patient; (3) a series of eight *z*-score maps, including two standardized axial sections defined by the ASPECTS method were then displayed next to the original CT images; (4) The observer viewed both the original CT images and the *z*-score maps and rated them again if the ratings were different from the first ones.

When reviewing on the monitor, a continuous rating scale was displayed for each location with a 100-point scale, the left, right end, and the center of which indicates "definitely absent", "definitely present" and "ambiguous", respectively. The indicator was originally set at the point of 50 (ambiguous) before an initial rating. The observers were permitted to review the entire sequence of CT slices of each patient and were also allowed to adjust window width and center level settings as necessary. Reading time was not limited in this study.

To evaluate observers' performance in the quantification of the extent of hypoattenuation regions without and with the *z*-score maps using the ASPECTS score system, we calculated the accuracy of quantification. The accuracy was defined as the sum of true-positive and true-negative regions per 10 ASPECTS-defined regions in each patient. A positive finding and a negative finding were assumed to be a point of higher than 50 and a point of less than 50, respectively, on a 100-point confidence rating scale. The point of 50 considered as ambiguous was initially indicated on a bar. The difference between the average accuracy values obtained without and with the *z*-score maps was estimated using a paired Student *t* test.

Observers' performance in the detection of focal hypoattenuation for the 210 regions without and with the *z*-score map was evaluated using receiver operating characteristic (ROC) analysis. A computer program (ROCKIT 0.9B; C. E. Metz, University of Chicago, Ill., USA) was used for obtaining binormal ROC curves from the continuous rating data (Uozumi et al., 2001). The statistical significance of the difference in the areas under these curves (AUC) obtained without and with *z*-score maps was tested by use of the jackknife method that involves an analysis of variance approach (Dorfman et al. 1992). A computer program (LABMRMC; C. E. Metz, University of Chicago, Ill., USA) was used for the test.

In the detection of focal hypoattenuation, average sensitivities and specificities without and with the *z*-score map were calculated. The statistical significances of the difference in the

sensitivities and the specificities without and with the *z*-score map were evaluated using the Wilcoxon matched-pairs signed-ranks test. Moreover, to validate the usefulness of the *z*-score mapping method, we determined the change in observers' findings without and with the *z*-score map in the detection of focal hypoattenuation. We assumed that a "clinically reverse action" in confidence levels occurred only when a finding was reversed between first and second ratings on the 100-point confidence rating scale. In hypoattenuation regions, a change from a negative finding or ambiguous to a positive finding implied that the use of the *z*-score map was beneficial. Similarly, a change from a positive finding or ambiguous to a negative finding implied that the use of the map was detrimental. In normal regions, inversely, a change from a positive finding or ambiguous to a negative finding implied that the use of the *z*-score map was beneficial. Similarly, a change from a negative finding or ambiguous to positive finding implied that the use of the map was detrimental. We calculated the number of regions in which the use of the *z*-score map led the observers to take the clinically reverse actions among the 210 regions. The differences between the median numbers of the clinically reverse actions without and with the use of the *z*-score maps for the five observers were evaluated using the Wilcoxon matched-pairs signed-ranks test. In all the analyses, a P value of less than 0.05 was considered to indicate a significant difference.

The average accuracy of the five observers for the quantification of the extent of hypoattenuation regions obtained without and with the *z*-score maps were 82.6% and 86.6%, respectively, indicating a significant difference (P<0.0001). Table 3 shows the accuracy values for the five observers without and with the *z*-score maps. Note that all observers improved the accuracies when viewing the *z*-score maps.

Observer	Without *Z*-Score Maps	With *Z*-Score Maps
A	77.6%	80.0%
B	77.6%	84.8%
C	85.2%	87.6%
D	88.1%	92.4%
E	84.3%	88.1%
Mean	82.6%	86.6% ($P < 0.0001$)

Table 3. Accuracy values for 5 neuroradiologists in quantification of the extent of hypoattenuation regions.

The average ROC curves for the five observers in the detection of focal hypoattenuation from the 210 regions without and with the *z*-score map are shown in Fig.15. The average AUC value was increased from 0.883 to 0.925 when the observers viewed the original CT images together with the *z*-score maps, and this difference was statistically significant (P=0.01). Table 4 shows the AUC values for the five observers without and with the *z*-score maps. Note that all observers improved the performance when viewing the *z*-score maps.

The average sensitivity in the detection of focal hypoattenuation was improved significantly from 80.6% (274 of 340 regions) to 88.8% (303 of 340 regions) by using the *z*-score map (P=0.042). The 340 regions were the product of the 68 hypoattenuation regions and five readings by the observers. The average specificity was improved from 77% (547 of 710 observations) to 80.4% (571 of 710 observations) when the observers used the *z*-score maps. The 710 observations were the product of the 142 normal regions and five readings by the

observers. No significant difference in the specificities between without and with the *z*-score maps was found (P=0.13).

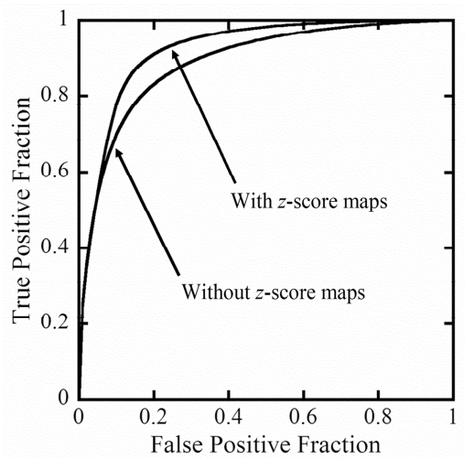

Fig. 15. Average receiver operating characteristic curves for five observers in the detection of focal hypoattenuation without and with the *z*-score map.

Observer	Without *Z*-Score Maps	With *Z*-Score Maps
A	0.843	0.898
B	0.925	0.955
C	0.925	0.938
D	0.903	0.938
E	0.822	0.894
Mean	0.883	0.924 ($P = 0.01$)

Table 4. AUC values for 5 neuroradiologists in the detection of focal hypoattenuation.

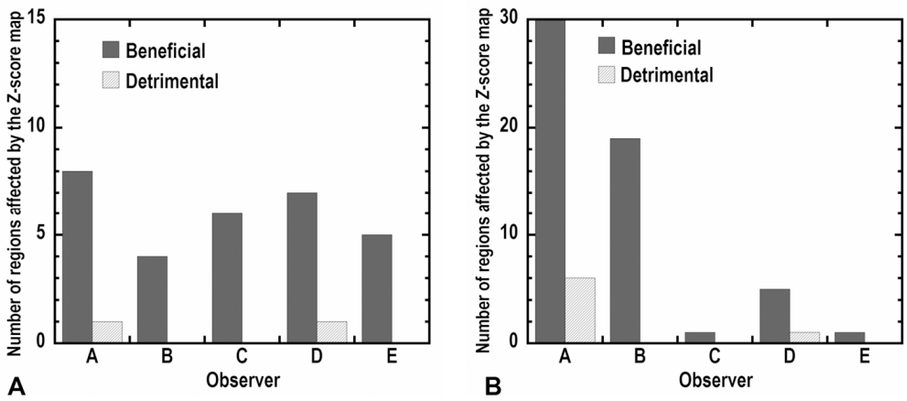

Fig. 16. Number of regions affected by the use of *z*-score maps in confidence levels with regard to hypoattenuation regions and normal regions. (A) hypoattenuation regions and (B) normal regions. The letters A-E on x-axis represent the five neroradiologists.

The results of the clinically reverse action in confidence levels for the observers are shown in Fig.16. In the hypoattenuation regions, the median number of the regions affected beneficially and that of the regions affected detrimentally were six and zero, respectively, which indicated a significant difference (P=0.04). Similarly, in the normal regions, the median number of the regions affected beneficially and that of the regions affected detrimentally were five and zero, respectively, which indicated a significant difference (P=0.04).

We evaluated the usefulness of the *z*-score mapping method on quantifying the extent of hypoattenuation regions of hyperacute stroke within 3 hours after onset of stroke ictus. The results showed that the neuroradiologists' performance in the quantification of the extent of hypoattenuation regions was improved significantly in patients with the MCA territory infarction by use of the method. So far little work has focused on improving radiologists' performance in the quantification of the extent of hypoattenuation areas by an image-processing approach. Until recently, a noise reduction filter for the increase in visualization of subtle hypoattenuation on nonenhanced CT images has been reported (Takahashi et al. 2007, 2008,; Lee et al. 2007). As a result, the performance of radiologists in the detection of hypoattenuation could be improved. However, not only the detection of hypoattenuation, but the quantification of the extent of hypoattenuation areas is important for the diagnosis and management of acute ischemic stroke. When the ASPECTS method is applied to quantify the extent of hypoattenuation regions, the existence of focal hypoattenuation at each of the 10 ASPECTS-defined locations needs to be accurately identified. Our observer performance test results indicated that the *z*-score map could significantly improve neuroradiologists' confidence levels in identifying the existence of focal hypoattenuation. This result may be an evidence to support the fact that the *z*-score mapping method would enable the neuroradiologists to improve the accuracy for the quantification of the extent of hypoattenuation regions.

The results of the clinically reverse action in confidence levels showed that the number of regions affected beneficially was significantly larger than that affected detrimentally in both the hypoattenuation regions and the normal regions. This result indicated that the use of *z*-score map could be useful in helping interpreters avoid miss interpretation of focal hypoattenuation. Figures 17 and 18 demonstrate two examples of the use of the *z*-score maps. In the case of Fig.17, the use of *z*-score maps prevented three of the five neuroradiologists from missed identification of focal hypoattenuation. Similarly, in the case of Fig.18, four of the five observers avoided the missed identification when using the *z*-score maps. Thus, we believe that the method could help neuroradiologists much in quantifying the extent of hypoattenuation of hyperacute stroke in this study.

There were differencies between our observer test and the clinical environment. First, No patients with old cerebral infarction were included in this study. No matter whether a low-density area of infarcts on unenhanced CT images is fresh or not, the area becomes a high-signal area on *z*-score maps. Therefore, recognizing a recent hypoattenuation area among high-signal areas on *z*-score maps is considerably difficult. However, since high-signal areas on *z*-score maps make interpreters aware that the corresponding areas on the unenhanced CT images might indicate the presence of low density areas, then the interpreter would observe the specific areas on the CT images to justify whether they are acute infarct areas or not. Next, only one patient with leuko-araiosis was included in this study, although many elderly patients with leuko-araiosis are examined by emergency CT scans in a clinical setting. In general, distinguishing a hypoattenuation area of embolic infarction involving cerebral cortex from leuko-araiosis would not be difficult, because low-density areas of

leuko-araiosis appear in the cerebral white matter. In this observer test, patients with embolic infarction were treated. Therefore, we believe that leuko-araiosis would not affect the observers' performance in the quantification of the extent of hypoattenuation regions in this study. However, the differentiation between leuko-araiosis and thrombotic infarction might be difficult, because thrombotic infarction often tends to spare the cortices. To further clarify the usefulness of *z*-score mapping, a study including patients with leuko-araiosis and thrombotic infarction will be needed. Practically, imaging studies in acute stroke may be interpreted by non-experts in emergency departments. It has been reported that both the sensitivity for the detection of acute stroke and the inter-rater homogeneity for the identification of lesion extent by non-experts were lower than those by experts in unenhanced CT imaging in the clinical situation (non-experts/experts: sensitivity, 41/61%; κ=0.38/0.51) (Fiebach et al. 2002). We examined the validity of the *z*-score mapping method in the interpretation by neuroradiologits but not by non-experts.

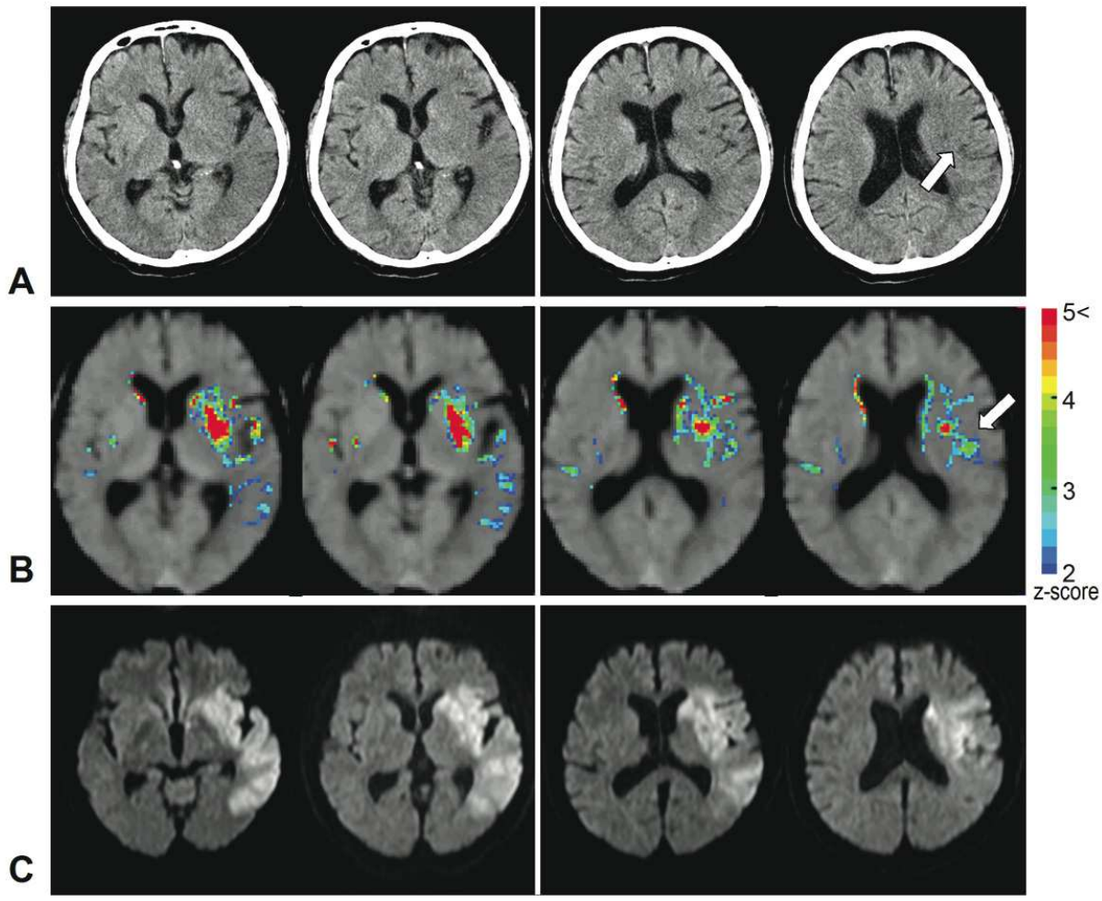

Fig. 17. 62-year-old-man with the right hemiplegia at 3 hours after stroke onset. (A) Unenhanced CT images show that parenchymal hypoattenuation at the left lentiform nucleus, caudate nucleus, temporal lobe, inferior parietal and posterior temporal lobe, and, precentral and superior frontal lobe (an arrow). (B) Z-score maps prevented three observers from missed identification of hypoattenuation at precentral and superior frontal lobe (an arrow); *z*-scores are indicated by a color bar (*right*). (C) Diffusion-weighted MR images taken after the first CT scan reveal hyperintense areas in the left MCA distribution.

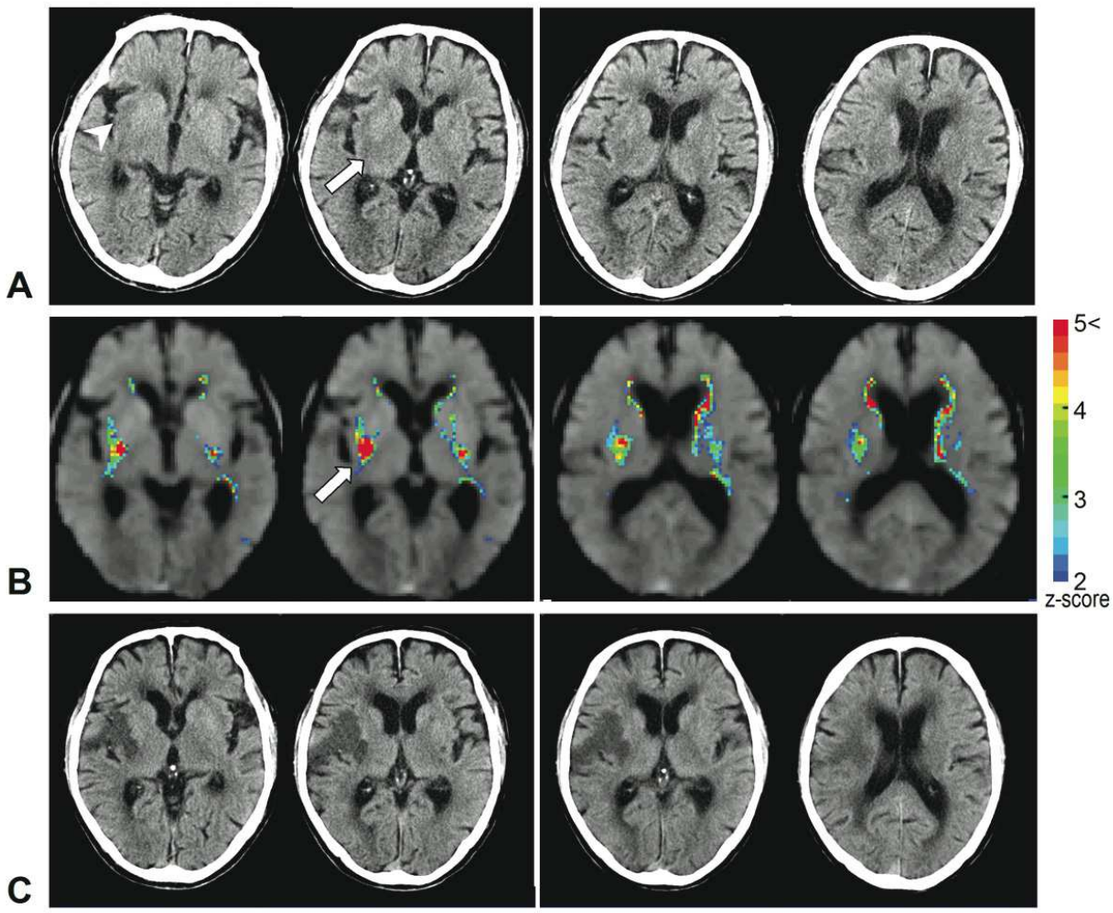

Fig. 18. 92-year-old-man with left hemiplegia at 1.3 hours after stroke onset. (A) Unenhanced CT images show that parenchymal hypoattenuation at the right lentiform nucleus (an arrow) and insula (an arrow head). (B) The *z*-score maps enabled four observers to avoid missing hypoattenuation at the right lentiform nucleus (a white arrow). A high-signal area is also seen within lacunar infarct in the left lentiform nucleus on the *z*-score maps, and moreover, a high-signal area which might be due to inaccurate normalization of enlarged cerebral ventricle appears at the left periventricular region on the *z*-score maps. Z scores are indicated by a color bar (*right*). (C) Follow-up CT images obtained one day after ictus demonstrate hypodense areas in the right MCA distribution.

In consideration that the method could improve the performance of the neuroradiologists who are expert in the diagnosis of acute stroke, we suppose that it might improve even better non-experts' performance in the quantification of the extent of hypoattenuation regions, and might serve as a useful tool for the diagnosis of acute stroke in emergency departments, but this issue remains to be studied further. The execution time required for processing of *z*-score mapping, including normalization, image processing and map display with a personal computer, was approximately six minutes. Data transfer implementations for the processing were performed manually in this study. We are working on constructing a fully automated *z*-score mapping system to further reduce the execution time. Indeed, it might take a longer time for the diagnosis with *z*-score maps in a clinical

situation. However, interpreters review mainly original, unenhanced CT images and refer the *z*-score maps as a "second opinion". We believed that the use of the *z*-score mapping method would not significantly increase the reading time.
In conclusion, the *z*-score mapping method has the potential to assist neuroradiologists to quantify the extent of hypoattenuation regions of hyperacue stroke on unenhanced CT images.

4. Conclusion

Two fundamental schemes to enhance/detect early CT signs were introduced. The enhancement technique was based on adaptive partial medial filter (APMF). The APMF was compared to 14 conventional denoising filters, and the results clearly demonstrated the superiority of the APMF. An observer test was performed to evaluate clinical value of whether the APMF was able to enhance hypoattenuation regions in nonenhanced CT images. As a result, all observers could improve their diagnostic performances, when the APMF image was used. The detection technique of early CT signs was based on *z*-score mapping method. The *z*-score mapping was able to distinctly visualize/detect hypoattenuation regions in CT images. Five neuroradiologists observed CT images together with the *z*-score mapping images to diagnose hyper acute stroke. As a result, the diagnostic accuracy was significantly improved when they referred to the *z*-score mapping images. In conclusion, the introduced two schemes would aid the clinical diagnosis of hyper acute stroke using nonenhanced CT images. In future works, we will introduce a knowledge based classification technique such as artificial neural network, fuzzy logic, etc., in order to develop intelligent computer-aided diagnosis system for cerebral acute stroke. We hope that the current and future techniques contribute to the improvement of diagnostic accuracy for acute stroke.

5. References

(2002). *The World Health Report 2002*, World Health Organization, pp. (186-191), ISBN 9241562072, Retrieved from < http://www.who.int/whr/2002/en/>

(2004). *Journal of Health and Welfare Statistics*, Health and Welfare Statistics Association, Vol.51, No.12, (October 2004).

Adams, H.; Adams, R.; Brott, T.; Zoppo, G.; Furlan, A.; Goldstein, L.B.; et al. (2003). Guidelines for the early management of patients with ischemic stroke: A scientific statement from the Stroke Council of the American Stroke Association. *Stroke*, Vol.34, pp. (1056-1083)

Adams, H.; Adams, R.; Zoppo, G. & Goldstein L.B. (2005). Guidelines for the early management of patients with ischemic stroke: 2005 guidelines update a scientific statement from the Stroke Council of the American Heart Association/American Stroke Association. *Stroke*, Vol.36, pp. (916-923)

Kummer, R.; Allen, K.L.; Holle, R.; Bozzao, L.; Bastianello, S.; Manelfe, C.; et al. (1997). Acute stroke: usefulness of early CT findings before thrombolytic therapy. *Radiology*, Vol.205, pp. (327-333)

Wardlaw, J.M.; Dorman, P.J.; Lewis, S.C. & Sandercock P.A. (1999). Can stroke physicians and neuroradiologists identify signs of early cerebral infarction on CT ?. *Journal of Neurology, Neurosurgery & Psychiatry*, Vol.67, pp. (651-653)

Barber, P.A.; Demchuk, A.M.; Zhang, J. & Buchan A.M. (2000). Validity and reliability of a quantitative computed tomography score in predicting outcome of hyperacute stroke before thrombolytic therapy. ASPECTS Study Group. Alberta Stroke Programme Early CT Score. *Lancet*, Vol.355, pp. (1670-1674)

Tomura, N.; Uemura, K.; Inugami, A.; Fujita, H.; Higano, S. & Shishido F. (1988). Early CT finding in cerebral infarction: obscuration of the lentiform nucleus. *Radiology*, Vol.168, pp. (463-467)

Truwit, C.L.; Barkovich, A.J.; Gean-Marton, A.; Hibri, N. & Norman D. (1990). Loss of the insular ribbon: another early CT sign of acute middle cerebral artery infarction. *Radiology*, Vol.176, pp. (801-806)

Schriger, D.L.; Kalafut, M.; Starkman, S.; Krueger, M. & Saver J.L. (1998). Cranial computed tomography interpretation in acute stroke: physician accuracy in determining eligibility for thrombolytic therapy. *Journal of American Medical Association*, Vol.279, pp. (1293-1297)

Wardlaw J.M. & Mielke O. (2005). Early signs of brain infarction at CT: observer reliability and outcome after thrombolytic treatment-systematic review. *Radiology*, Vol.235, pp. (444-453)

Kalender W.A. (2000). *Computed Tomography: Fundamentals, System Technology. Image Quality and Applocations*, Wiley-VCH, ISBN 3895780812, Munich, Germany

Kalra, M.K.; Maher, M.M. ; Sahani, D.V. ; Blake, M.A. ; Hahn, P.F. ; Avinash, G.B. ; et al. (2003). Low-dose CT of the abdomen: evaluation of image improvement with use of noise reduction filters-pilot study. *Radiology*, Vol.228, pp. (251-256)

Kachelriess, M.; Watzke, O. & Kalender W.A. (2001). Generalized multi-dimensional adaptive filtering for conventional and spiral single-slice, multi-slice, and cone-beam CT. *Medical Physics*, Vol.28, pp. (475-490)

Lee, Y.; Takahashi, N.; Tsai, D.Y. & Ishii, K. (2007). Adaptive partial median filter for early CT signs of acute cerebral infarction. *International Journal of Computer Assisted Radiology and Surgery*, Vol.2, No.2, pp. (105-115)

Guis, V.H.; Adel, M.; Rasigni, M. & Rasigni G. (2003), Adaptive neighborhood contrast enhancement in mammographic phantom images. *Optical Engineering*, Vol.42, pp. (357-366)

Tsai, D.Y.; Takahashi, N. & Lee Y. (2005). An Adaptive Enhancement Algorithm for CT Brain Images. *Proceedings of the 2005 IEEE Engineering in Medicine and Biology 27th Annual Conference*, paper #124

Lee, Y.; Takahashi, N.; Tsai, D.Y. & Fujita H. (2006). Detectability improvement of early sign of acute stroke on brain CT images using an adaptive partial smoothing filter. *Proceedings of SPIE Medical Imaging*, Vol.6144, pp. (2138-2145)

Takahashi, N.; Lee, Y.; Tsai, D.Y. & Ishi, K. (2007). A novel noise reduction filter for improving visibility of early CT signs of hyperacute stroke: evaluation of the filter's performance - preliminary clinical experience-. *Radiation Medicine*, Vol.25, No.3, pp. (247-254)

Russ, J.C. (1995). *The Image Processing Handbook* (2nd edition), pp. (155-178), CRC Press, ISBN 0849325323, Boca Raton, USA.

Tukey, J.W. (1971). *Exploratory Data Analysis*. Addison Wesley, ISBN 0201076160,

Davis, L.S. & Rosenfeld, A. (1978). Noise cleaning by iterated local averaging. *IEEE Transactions on Systems, Man and Cybernetics*, Vol.SMC-8, pp. (705-710)

Wu, W.Y.; Wang, M.J J. & Liu, C.M. (1992). Performance evaluation of some noise reduction methods. *Comput Vision Graphics and Image Processing*, Vol.54, pp. (134-146).

Ehrich, R.W. (1978). A symmetric hysteresis smoothing algorithm that preserves principal features. *Comput Graphics and Image Processing*, Vol.8, pp. (121-126)

Lev, A.; Zucker, S.W. & Rosenfeld, A. (1977). Iterative enhancement of noisy images. *IEEE Transactions on Systems, Man and Cybernetics*, Vol.SMC-7, pp. (435-442)

Wang, D.C.C.; Vagnucci, A.H., & Li, C.C. (1981). Gradient inverse weighted smoothing scheme and the evaluation of its performance. *Comput Vision Graphics and Image Processing*, Vol.15, pp. (167-181)

Nagao, M. & Matuyama, T. (1978). Edge Preserving smoothing. *Comput Graphics and Image Processing*, Vol.9, pp. (394-407)

Zamperoni, P. (1990). Some Adaptive Rank Order Filters for Image Enhancement. *Pattern Recognition Letters*, Vol.11, pp. (81-86)

Xu, X.; Miller, E.L.; Chen, D. & Sarhadi, M. (2004). Adaptive Two-Pass Rank Order Filter to Remove Impulse Noise in Highly Corrupted Images. *IEEE Transactions on Image Processing*, Vol.13, No.2, pp. (238-247)

Kuan, D.T.; Sawchuk, A.A, Strand, T.C & Chavel, P. (1985). Adaptive Noise Smoothing Filter for Images with Signal-Dependant Noise. *IEEE Transactions on Pattern Analysis and Machine Intelligence*, Vol.7, No.2, pp. (165-177)

Centeno, J.A.A & Haertel, V. (1997). An Adaptive Image Enhancement Algorithm. *Pattern Recognition*, Vol.30, No.7, pp. (1183-1189)

Fischl, B. & Shwartz, E.L. (1999). Adaptive Nonlocal Filtering: A Fast Alternative to Anisotropic Diffusion for Image Filtering. *IEEE Transactions on Pattern Analysis and Machine Intelligence*, Vol.21, No.1, pp. (42-48)

Westin, C.F.; Richolt, J.; Moharir, V. & Kikinis, R. (2000). Affine Adaptive Filtering of CT Data. *Medical Image Analysis*, Vol.4, No.2, pp. (161-177)

Schilham, A.M.R.; Ginneken, B.V. ; Gietema, H. & Prokop, M. (2006). Local Noise Weighted Filtering for Emphysema Scoring of Low-Dose CT Images. *IEEE Transactions on Medical Imaging*, Vol.25, No.4, pp. (451-463)

Gijbels, I.; Lambert, A. & Qiu P. (2006). Edge-Preserving Image Denoising and Estimation of Discontinuous Surfaces. *IEEE Transactions on Pattern Analysis and Machine Intelligence*, Vol.28, No.7, pp. (1075-1087)

Lev, M.H.; Farkas, J.; Gemmete, J.J., Hossain, S.T. ; Hunter, G.J.; Koroshetz, W.J. & Gonzalez, R.G. (1999). Acute stroke: improved nonenhanced CT detection-benefits of soft-copy interpretation by using variable window width and center level settings. *Radiology*, Vol.213, pp. (150-155)

Dolfman, D.D.; Berbaum, K.S. & Metz C.E. (1992). ROC rating analysis: generalization to the population of readers and cases with the jackknife method. *Investigative Radiology*, Vol.27, pp. (723–731)

Kalafut, M.A.; Schriger, D.L.; Saver J.L. & Starkman, S. (2000). Detection of early CT signs of >1/3 middle cerebral artery infarctions: interrater reliability and sensitivity of CT interpretation by physicians involved in acute stroke care. *Stroke*, Vol.31, pp. (1667-1671)

Fiebach, J.B.; Schellinger, P.D.; Jansen, O.; Meyer, M; Wilde, P.; Bender, J.; Schramm, P.; Juttle, E.; Oehler, J.; Hartmann, M.; Hahnel, S.; Knauth, M.; Hacke, W. & Sartor, K. (2002). CT and diffusion-weighted MR imaging in randomized order: diffusion-

weighted imaging results in higher accuracy and lower interrater variability in the diagnosis of hyperacute ischemic stroke. *Stroke*, Vol.33, pp. (2144-2155)

Camargo, E.C.S.; Furie, K.L.; Singhal, A.B.; Roccatagliata, L.; Cunnane, M.E.; Halpern, E.F.; Harris, G.J.; Smith, W.S.; Gonzalez, R.G.; Koroshetz, W.J. & Lev, M.H. (2007). Acute brain infarct: detection and delineation with CT angiographic source images versus nonenhanced CT scans. *Radiology*, Vol.244, pp. (541-548)

Takahashi, N.; Tsai, D.Y.; Lee, Y.; Kinoshita, T. & Ishii, K. (2010). Z-score mapping method for extracting hypoattenuation areas of hyperacute stroke in unenhanced CT. *Academic Radiology*, Vol.17, No.1, pp. (84-92)

Takahashi, N.; Tsai, D.Y.; Lee, Y.; Kinoshita, T.; Ishii, K.; Tomaru, H. & Takahashi, S. (2010). Usefulness of z-score mapping for quantification of extent of hypoattenuation regions of hyperacute stroke in unenhanced computed tomography: analysis of radiologist's performance. *Journal of Comupter Assited Tomography*, Vol.34, No.5, pp. (751-756)

Friston, K.J.; Ashburner, J.; Frith, C.D.; Poline, J.B.; Heather, J.D. & Frackowiak, R.S.J. (1995). Spatial registration and normalization of images. *Human Brain Mapping*, Vol.3, No.3, pp. (165-189)

Ashburner, J. & Friston, K.J. (1999). Nonlinear spatial normalization using basis functions. *Human Brain Mapping*, Vol.7, No.4, pp. (254-266)

Uozumi, T.; Nakamura, K.; Watanabe, H.; Nakata, H.; Katsuragawa, S. & Doi, K. (2001). ROC analysis on detection of metastatic pulmonary nodules on digital chest radiographs by use of temporal subtraction. *Academic Radiology*, Vol.8, No.9, pp. (871-878)

Metz, C.E.; Herman, B.A. & Shen, J.H. (1998). Maximum likelihood estimation of receiver operating characteristic (ROC) curves from continuously-distributed data. *Statistics in Medicine*, Vol.17, No.9, pp. (1033-1053)

Takahashi, N.; Lee, Y.; Tsai, D.Y. & Ishii, K. (2008). Improvement of detection of hypoattenuation in sensitive ischemic stroke in unenhanced CT using an adaptive smoothing Filter. *Acta Radiologica*, Vol.49, No.7, pp. (816-826)

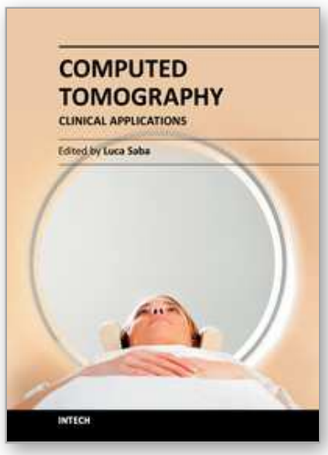

Computed Tomography - Clinical Applications
Edited by Dr. Luca Saba

ISBN 978-953-307-378-1
Hard cover, 342 pages
Publisher InTech
Published online 05, January, 2012
Published in print edition January, 2012

Computed Tomography (CT), and in particular multi-detector-row computed tomography (MDCT), is a powerful non-invasive imaging tool with a number of advantages over the others non- invasive imaging techniques. CT has evolved into an indispensable imaging method in clinical routine. It was the first method to non-invasively acquire images of the inside of the human body that were not biased by superimposition of distinct anatomical structures. The first generation of CT scanners developed in the 1970s and numerous innovations have improved the utility and application field of the CT, such as the introduction of helical systems that allowed the development of the "volumetric CT" concept. In this book we want to explore the applications of CT from medical imaging to other fields like physics, archeology and computer aided diagnosis. Recently interesting technical, anthropomorphic, forensic and archeological as well as paleontological applications of computed tomography have been developed. These applications further strengthen the method as a generic diagnostic tool for non- destructive material testing and three-dimensional visualization beyond its medical use.

How to reference
In order to correctly reference this scholarly work, feel free to copy and paste the following:

Yongbum Lee, Noriyuki Takahashi and Du-Yih Tsai (2012). Computer-Aided Diagnosis for Acute Stroke in CT Images, Computed Tomography - Clinical Applications, Dr. Luca Saba (Ed.), ISBN: 978-953-307-378-1, InTech, Available from: http://www.intechopen.com/books/computed-tomography-clinical-applications/computer-aided-diagnosis-for-acute-stroke-in-ct-images

INTECH
open science | open minds

InTech Europe
University Campus STeP Ri
Slavka Krautzeka 83/A
51000 Rijeka, Croatia
Phone: +385 (51) 770 447
Fax: +385 (51) 686 166
www.intechopen.com

InTech China
Unit 405, Office Block, Hotel Equatorial Shanghai
No.65, Yan An Road (West), Shanghai, 200040, China
中国上海市延安西路65号上海国际贵都大饭店办公楼405单元
Phone: +86-21-62489820
Fax: +86-21-62489821

IntechOpen